Ultrafast Electrical Measurements of Isolated Silicon Nanowires and Nanocrystals

7 AUTHORS, INCLUDING:

Matthew R Bergren
UbiQD, LLC
8 PUBLICATIONS **60** CITATIONS

SEE PROFILE

Chito E. Kendrick
Colorado School of Mines
38 PUBLICATIONS **305** CITATIONS

SEE PROFILE

Thomas E Furtak
Colorado School of Mines
158 PUBLICATIONS **2,463** CITATIONS

SEE PROFILE

Matthew C Beard
National Renewable Energy Laboratory
114 PUBLICATIONS **7,874** CITATIONS

SEE PROFILE

Ultrafast Electrical Measurements of Isolated Silicon Nanowires and Nanocrystals

Matthew R. Bergren,[†,‡] Chito E. Kendrick,[†,§] Nathan R. Neale,[‡] Joan M. Redwing,[§] Reuben T. Collins,[†] Thomas E. Furtak,[†] and Matthew C. Beard*[,†,‡]

[†]Physics Department, Colorado School of Mines, Golden, Colorado 80401, United States

[‡]Chemical and Materials Science Center, National Renewable Energy Laboratory, Golden, Colorado 80401, United States

[§]Materials Science and Engineering Department, Penn State University, State College, Pennsylvania 16801, United States

Ⓢ *Supporting Information*

ABSTRACT: We simultaneously determined the charge carrier mobility and picosecond to nanosecond carrier dynamics of isolated silicon nanowires (Si NWs) and nanocrystals (Si NCs) using time-resolved terahertz spectroscopy. We then compared these results to data measured on bulk c-Si as a function of excitation fluence. We find >1 ns carrier lifetimes in Si NWs that are dominated by surface recombination with surface recombination velocities (SRV) between ~1100−1700 cm s^{-1} depending on process conditions. The Si NCs have markedly different decay dynamics. Initially, free-carriers are produced, but relax within ~1.5 ps to form bound excitons. Subsequently, the excitons decay with lifetimes >7 ns, similar to free carriers produced in bulk Si. The isolated Si NWs exhibit bulk-like mobilities that decrease with increasing excitation density, while the hot-carrier mobilities in the Si NCs are lower than bulk mobilities and could only be measured within the initial 1.5 ps decay. We discuss the implications of our measurements on the utilization of Si NWs and NCs in macroscopic optoelectronic applications.

SECTION: Physical Processes in Nanomaterials and Nanostructures
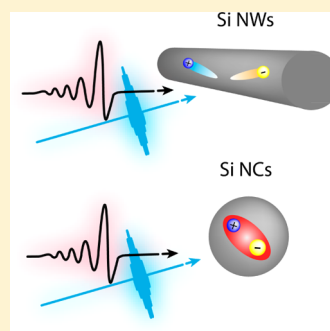
The incorporation of Si nanostructures into optoelectronic devices relies on the ability to study, understand, and control their optical and electrical properties. Although optical measurements such as transient absorption[1] and photoluminescence (PL)[2−4] are typical characterization techniques, it remains difficult to measure the average intrinsic electrical response of these small structures. One way to obtain electrical properties of Si nanostructures is to measure them in a thin film geometry with traditional[5] or noncontact electrical probes,[6−8] but such measurements reflect the response of the composite film and not necessarily that of the individual nanostructure. Traditional measurements can be made on individual nanowires, where the length of the wire is usually on the order of micrometers. For these nanostructures, ohmic contacts can be applied to the ends of the wire, and the electrical properties can be measured.[9−11] Unfortunately, in order to obtain the average electrical response of the nanowires, such measurements would need to be repeated many times, which would be a laborious task.

In this work, we employed a contactless electrical probe called time-resolved terahertz spectroscopy (TRTS) to measure the intrinsic photoconductivity of electrically isolated silicon nanowires (Si NWs) and silicon nanocrystals (Si NCs) dispersed in a solvent. The terahertz probe frequencies span typical carrier scattering rates, providing valuable information about the local charge carrier generation and transport characteristics. Unlike other ultrafast optical techniques such

as transient absorption[1,12] and transient PL,[13,14] which depend on interband optical transitions, TRTS is uniquely suited to study indirect bandgap semiconductors since the terahertz probe directly measures the free-carrier dynamics and is not sensitive to the indirect nature of the optical transitions. The TRTS measurements also provide the average electrical response of an individual Si NW or Si NC since the measurements are carried out on an ensemble of nanostructures. Here, we compare the carrier dynamics and extracted mobilities of the Si NWs, Si NCs, and bulk crystalline silicon (c-Si) and show how the electrical properties change between these three different forms of silicon.

We measured four different nanostructured silicon samples (3 types of Si NWs and 6.3 nm diameter Si NCs). The Si NWs were grown on a ⟨111⟩-oriented c-Si wafer by a vapor−liquid−solid (VLS) method. Detailed information on the NW synthesis is provided in the supplemental section. The as-grown Si NWs employed a gold catalyst seed and are 90 nm in diameter with a length of ~17 μm. The as-grown Si NWs were then divided into three groups (A, B, and C). In order to study the diameter dependence of the electrical properties of the Si NWs, the diameter of sample A was reduced to 30 nm. These smaller diameter wires were prepared by thermally oxidizing the

90 nm as-prepared Si NWs at 900 °C in the presence of O_2. The self-limiting oxidation[15] results in 30 nm SiO_2 shell and a 30 nm c-Si core diameter for the Si NWs. The oxide was then etched with HF, leaving 30 nm Si NWs. For the second set of Si NWs (sample B), we annealed the as-prepared, 90 nm diameter NWs in an argon atmosphere, also at 900 °C. These two samples were then compared to the as-prepared wires (sample C), which did not undergo any postsynthesis treatments. Before the TRTS measurements were made, each NW sample was etched with HF to remove any SiO_2 remaining on the NW surface. To exclude the contributions from the underlying Si substrate, the NWs were also mechanically removed from the substrate, reducing the wire length to ∼10 μm. After removal, the wires were dispersed in chloroform, and the samples were stirred during the TRTS measurement to assist in maintaining the Si NW dispersion.

The 6.3 nm diameter Si NCs were synthesized by silane (SiH_4) decomposition in an RF-enhanced nonthermal plasma[4] (see Supporting Information for detailed information). The surfaces of Si NCs were functionalized with dodecyl ligands via hydrosilylation[16] allowing them to be dispersed into hexane for the terahertz measurements. The bulk c-Si sample was a 620 μm thick, (111)-oriented wafer that was double-side polished and slightly p-type doped, with a resistivity of 18 Ω cm.

TRTS is a visible pump, far-infrared probe (Figure 1) that simultaneously measures the real and imaginary parts of the frequency-dependent photoconductivity, $\tilde{\sigma}(\omega; \tau_p)$, with sub-picosecond time resolution (τ_p is the pump−probe delay time). In a TRTS measurement, there are two delays to consider (Figure 1); the pump−probe delay, τ_p, and the terahertz delay, t_{THz}. The relative change in transmitted terahertz electric field, $\Delta E(\tau_p, t_{THz})/E$ is measured as a function of both delays, where $\Delta E = E' - E$. The transmitted terahertz electric field with pump pulse on is represented by E', while E represents the transmitted terahertz electric field with pump pulse off (also referred to as the reference pulse). Thus, there are two types of TRTS measurements: (1) The carrier dynamics are measured by fixing the terahertz delay at the maximum value of the terahertz pulse, t_{max}, and scanning τ_p, yielding $\Delta E(\tau_p; t_{max})/E$ and (2) the frequency-dependent complex photoconductivity can be extracted by scanning t_{THz} for fixed values of τ_p, yielding,
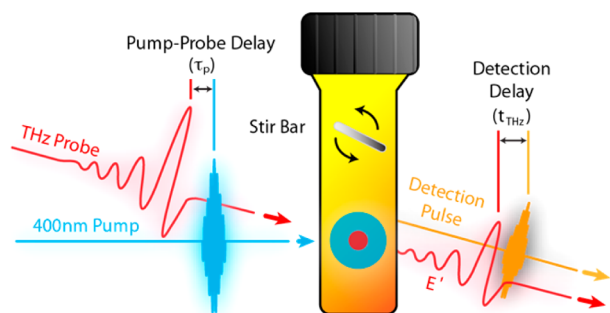

Figure 1. Schematic of the TRTS experiments. TRTS is a pump−probe measurement. In this experiment, the pump pulse is 400 nm with pulse duration of 100 fs and the probe light is a single cycle terahertz pulse. There are two delays in the TRTS experiment. The delay between the terahertz and pump pulse is τ_p and the delay between the transmitted terahertz pulse and the detection pulse is t_{THz}. The Si NCs or NWs are dispersed into hexane or chloroform and stored in a sealed cuvette and the samples are stirred during the measurements.

$\Delta E(t_{THz}; \tau_p)/E$. For the measurements here, a double modulation TRTS setup was employed, allowing for simultaneous acquisition of the reference and differential terahertz waveform and is described elsewhere.[17] The time-domain scans are then Fourier transformed into the frequency domain to obtain the complex frequency-dependent photoconductivity spectrum, $\tilde{\sigma}(\omega; \tau_p)$. In our experiment, we used a 400 nm (3.1 eV) photoexcitation pulse. In order to determine absolute values of the mobility and carrier density, we need to know how much light is absorbed by the nanostructures at 400 nm. The optical density values (OD) for the Si NWs at 400 nm are 0.09, 0.01, and 0.12 for sample A, B, and C, respectively, and 1.28 for the Si NC sample.

The average photoconductivity can be related to $\Delta E(\tau_p; t_{max})/E$ (for $\Delta E/E$ values less than ∼0.2)[18] by

$$\langle\sigma(\tau_p)\rangle = -\frac{\Delta E(\tau_p; t_{max})}{E}\frac{\varepsilon_0 c\beta}{zV_f}\kappa \tag{1}$$

where ε_0 is the permittivity of free space, c is the speed of light, β is a constant that depends on the experimental configuration, κ is a local field correction factor that accounts for small dielectric ellipsoids embedded in a low dielectric medium, and $\langle\rangle$ denotes averaging over all Si NWs/NCs, NW/NC geometries, and the terahertz frequency bandwidth. For high OD samples, z is the optical penetration depth and for the low OD samples, z is the thickness of the cuvette or sample. A derivation of eq 1 can be found in the supplemental section. For bulk c-Si, we considered the equations developed by Kužel et al. governing the propagation of terahertz pulses through a thick film with surface excitation,[19] yielding $\beta_{bulk} = (n_{si} + 1)^3/4n_{si}$, where n_{si} is the refractive index for bulk c-Si, z is the optical penetration depth of 400 nm light in bulk c-Si (∼100 nm), and $\kappa_{bulk} = 1$. For the Si NW samples, with low OD, $\beta_{NW} = (n_{chl} + n_q)^2/2n_q$ (see ref 19, eq 53) and z is the cuvette thickness of 2 mm. For the NC samples, with a higher OD, we find $\beta_{NC} = (n_{hex} + n_q)^3/4n_qn_{hex}$, and z is the optical penetration depth of ∼0.2 mm. The values for the index of refraction of chloroform (n_{chl}), quartz cuvette (n_q), and the hexane solution (n_{hex}) at terahertz wavelengths are 1.46,[20] 2.16,[21] and 1.42,[22] respectively. To extract the frequency-dependent photoconductivity, we utilized the frequency-space equivalent of eq 1.

To determine κ, we employed an effective media theory (EMT), since the wavelength of light corresponding to terahertz frequencies (∼100 μm to 2 mm) is much larger than the dispersed nanostructures. Work done by Giordano shows how an effective permittivity (ε_{eff}) of a dispersion of dielectric ellipsoids can be obtained using EMT where the dielectric ellipsoids, with permittivity ε_2, are embedded in a homogeneous matrix with permittivity ε_1. Both dilute and concentrated dispersions were considered as well as oriented and randomly oriented ellipsoids.[23] In our study, the dispersion consists of dilute randomly oriented cylindrical rods (Si NWs) and dilute spheres (NCs). For the case of the NWs, solving eq 25 from ref 19 for the effective permittivity with depolarization factors of 1/2 for the axes orthogonal to the NW axis and zero along the axis results in

$$\varepsilon_{eff} = \varepsilon_1 + \frac{V_f}{3}\cdot\frac{\varepsilon_1(\varepsilon_2 - \varepsilon_1)(5\varepsilon_1 + \varepsilon_2)}{\varepsilon_1 + \varepsilon_2} \tag{2}$$

where V_f is the volume fraction of the embedded ellipsoids, ε_1 is the permittivity of the suspending medium, and ε_2 is the permittivity of the embedded ellipsoids. The effective

permittivity for a dilute dispersion of spheres can be written as $\varepsilon_{\text{eff}} = \varepsilon_1 + 3V_f\varepsilon_1^2(\varepsilon_2 - \varepsilon_1)/(2\varepsilon_1 - \varepsilon_2)$. Using these values for the effective permittivity of the NWs and NCs, we find (see Supporting Information for derivation),

$$\kappa_{\text{NW}} = 3(\varepsilon_1 + \varepsilon_2)/2\varepsilon_1(2\varepsilon_1 + \varepsilon_2) \tag{3}$$

and

$$\kappa_{\text{NC}} = (2\varepsilon_1 + \varepsilon_2)/3\varepsilon_1^2 \tag{4}$$

where $\varepsilon_1 = 2.13$ is the permittivity of the suspending medium (chloroform),[22] and $\varepsilon_2 = 11.7$ is the permittivity of the embedded Si NWs.[21] For the Si NC case, $\varepsilon_1 = 2.02$[22] is the permittivity of hexane, and $\varepsilon_2 = 9.61$ is the modified permittivity value for a Si NC calculated according to the Penn model.[24] In general, κ is both complex and frequency-dependent; however, in these experiments, the solvents and NCs do not absorb significant terahertz light in their ground state and the frequency-dependence is minimal. We determined V_f of each sample from the OD of the Si nanostructure suspensions (see Supporting Information), and V_f of each sample is 2.66×10^{-6}, 2.89×10^{-7}, and 3.47×10^{-6} for Si NW samples A, B, and C, respectively, and 1.06×10^{-3} for the NC sample.

Carrier Dynamics. In Figure 2 we display the carrier dynamics for each of the five samples. Figure 2a shows the photoconductivity for the NW samples under conditions that produce identical initial carrier densities, n_0. In Figure 2b, we display the normalized $\sigma(\tau_p)$ of the 6.3 nm Si NCs and compare them to the normalized signals of the 30 nm Si NWs (sample A), as well as bulk c-Si.

The photoconductivity of a material depends on the product of the mobility and carrier density $\sigma(\tau_p) = e\mu(\tau_p)*N(\tau_p)$, where both the mobility and/or carrier density can be time-dependent. We consider two sources for a time-dependent mobility: (1) hot-carrier cooling and/or intervalley scattering and (2) the mobility is dependent on the carrier density, which is itself time-dependent. Hot-carrier cooling and intervalley scattering are only important at the earliest times ((τ_p) < 2 ps), whereas the mobility in Si only varies slightly with the change in carrier density (*vide infra*). We therefore only consider a time-dependent carrier density $\sigma(\tau_p) = e\mu* N(\tau_p)$. It is possible that time-dependent phase shifts in the terahertz waveform could contribute to changes in amplitude, but we find this effect to be less than 1% in our measurements. This is confirmed in Figure S5 where no apparent shift in the terahertz waveform for the Si NCs is observed for delays up to 10 ps.

The photoconductivity is higher in the annealed NWs compared to the as-prepared NWs due to an enhanced mobility, since n_0 is constant for each sample. The carrier lifetime is shorter in the 30 nm annealed NWs compared to the 90 nm annealed NWs, because of a larger surface-to-volume ratio in the smaller diameter wires that presumably speeds carrier recombination. For the Si NCs we observe an initial rapid decrease in the photoconductivity followed by a long-lived signal, which lasts well past the 1 ns window of our experiment. The fast dynamics occur from a hot-carrier cooling process that is discussed below. The long-lived portion of the Si NC dynamics resembles the long lifetime observed for the bulk sample, while the Si NW dynamics are faster due to surface recombination, which suggests that the surface of the Si NCs is well passivated.

We measured $\sigma(\tau_p)$ as a function of excitation fluence and display the results for the three NW samples in Figure 3. The
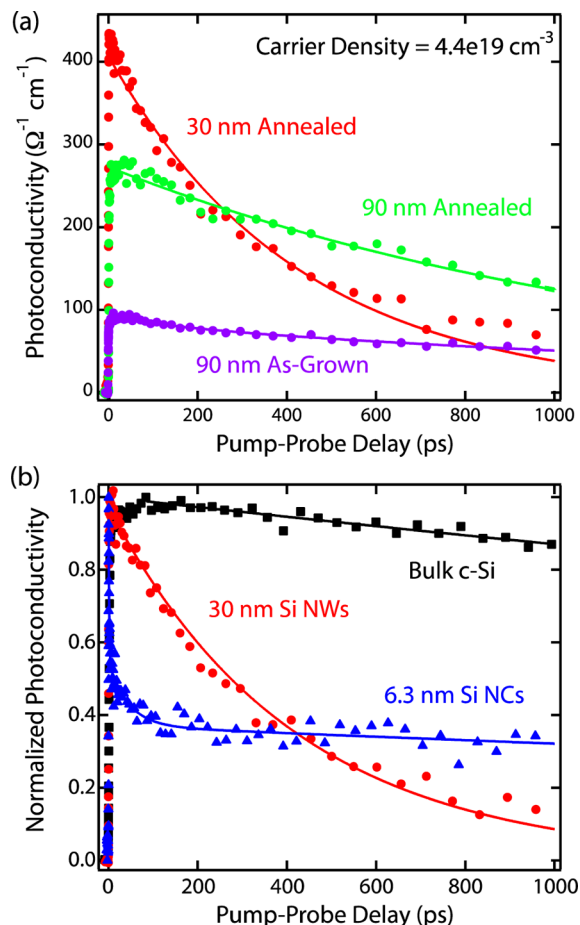

Figure 2. (a) Carrier dynamics of Si NWs measured at the same photoinduced carrier density (4.4×10^{19} cm^{-3}). The purple and green circles represent 90 nm diameter Si NWs for as-grown and Ar-annealed samples, respectively. The red circles represent annealed 30 nm diameter Si NWs. (b) Shows the normalized carrier dynamics of bulk c-Si (black squares), the 30 nm diameter Si NWs (red circles) and 6.3 nm Si NCs (blue triangles). Solid lines represent the models described in the text.

fluence dependent data for the NCs is shown in the Supporting Information (Figure S3). The normalized transients for the NW sample reveal a slight change in the carrier dynamics for sample C as the fluence was varied, while sample A and B displayed similar dynamics for all fluences measured (see Figure S2 in the Supporting Information). The NC dynamics also display a slight dependence on excitation fluence. We model the time-dependent carrier density for the Si NWs by solving the diffusion equation for an infinitely long cylinder with boundary conditions that incorporate a surface recombination velocity (SRV).[25] The resulting equation for the average photoconductivity of a Si NW is (see derivation in the Supporting Information)

$$\langle \sigma_{\text{NW}}(\tau_p) \rangle = n_0 e\mu_{\text{NW}}[(1 - f)e^{-2s\tau_p/a} + fe^{-\tau_p/\tau_1}] \tag{5}$$

where n_0 is the initial carrier density created by the pump pulse, a is the Si NW radius, s is the SRV, and μ_{NW} is the mobility of the wire at the peak of the transient. For each sample, the fluence-dependent data were globally modeled to extract values for μ_{NW} and s. In order to account for the observed fast decay in the as-prepared wires (τ_p < 100 ps),we include a second exponential decay term (τ_1) and scaling factor f, which is

2052

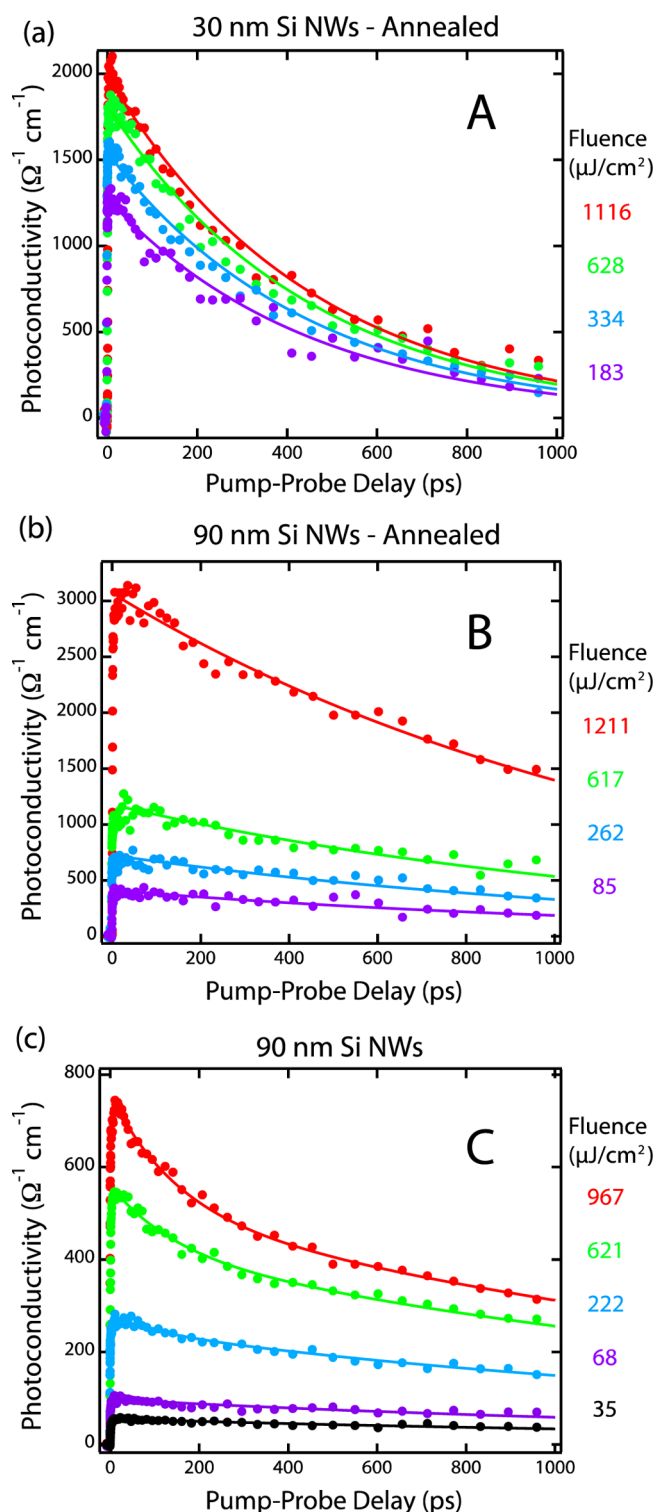dx.doi.org/10.1021/jz500863a | *J. Phys. Chem. Lett.* 2014, 5, 2050−2057

Figure 3. Fluence-dependent photoconductivity measurements on the thermally oxidized, 30 nm diameter Si NWs (a), the argon annealed 90 nm Si NWs (b), and the as-prepared 90 nm diameter Si NWs (c). The data are globally fit with a surface recombination model described in the text.

1. We find that the Si NW decay dynamics are completely governed by surface recombination. It is likely that annealing causes residual gold, initially located in the interior of the NW, to diffuse to the surface[26,27] leaving behind a higher quality Si NW core. Such a process could explain the higher SRV observed for the annealed wires compared to the as-prepared wires and the higher mobility measured in the annealed samples compared the as-prepared sample. Thus, annealing increases the quality of the core at the expense of the surface.

The nonlinear 150 ps decay observed in the as-prepared sample C could arise from an impurity related Auger process. Carrier−carrier Auger lifetimes in bulk c-Si have been observed to be ~1−2 ns at excess carrier densities of ~10^{19} cm^{-3},[28] which is considerably longer than the 150 ps decay measured here for similar carrier densities. One possible explanation is residual gold trapped inside the as-prepared NWs could mediate an excitonic Auger recombination process in the wires. In the excitonic Auger recombination model, an exciton encounters an impurity with a midgap energy level and either the electron or hole from the exciton is captured into the impurity level, giving up it is excess energy to the other charge.[29] Such a process could explain the ~150 ps decay observed here. The absence of the faster dynamics in the annealed samples (A and B) is consistent with our supposition that there is more gold in the interior of the as-prepared wires compared to the annealed wires (*vide supra*).

SRVs have been measured in Au-catalyzed, VLS-grown Si NWs samples, both in single NW device geometries[9−11] and in Si NW arrays on a c-Si substrate.[13] Single NW devices consisting of phosphorus-doped Si NWs exhibit SRVs of ~30 000 cm s^{-1}, which are attributed to defects associated with the native oxide that remains on the surface of the NW. In that study, SRVs increased by an order of magnitude as the NW diameter was varied from 93 to 35 nm.[9] In contrast, here we find the SRV only changes by 100 cm s^{-1} when the diameter varies from 90 to 30 nm. The dynamics of the 30 nm NWs compared to the 90 nm NWs is much faster (see Figure 2) even though the SRV is similar because there are more carriers near the surface in the smaller NWs.

Various researchers have attempted to reduce SRVs by applying different passivation schemes. By coating the Si NWs with a thin layer of a-Si, Dan et al. demonstrated a large reduction in the SRV of their Si NWs, from 30 000 cm s^{-1} for uncoated wires to ~4500 cm s^{-1} for the a-Si coated NWs.[10] Heating the NWs can effectively passivate the Si NWs via annealing of defects. SRVs calculated from measurements made on single NW Si solar cells are similar to the values reported here, with a maximum calculated SRV of ~1350 cm s^{-1}.[11] In those studies, the NWs were effectively passivated when electrically heated in order to produce rectifying junctions in the NW. In another study, low SRVs (~20 cm s^{-1}) were measured via time-resolved PL for thermally passivated Si NWs.[13] The NWs were first thermally oxidized at 960 °C (similar to our 30 nm Si NWs) and then annealed in a forming gas atmosphere at either 960 or 450 °C. In those measurements, the Si NWs were not detached from the underlying substrate, and it is unclear what effect the Si substrate plays in extracting SRVs.

We note that photoelectrical measurements on isolated nanostructures are easier to interpret and only reflect the properties of the nanostructure itself. For example, a careful study by Ulbricht et al. on Si NWs still attached to c-Si substrate, where they were able to successfully separate the

associated with the intensity dependent recombination. In the global fit, *f* was allowed to vary with pump fluence for sample C and was zero for samples A and B. The values of *f* ranged from 0.01 to 0.33 for the as-prepared wires and τ_1 was a global variable in the model. The best-fit values are reported in Table

2053

dx.doi.org/10.1021/jz500863a | *J. Phys. Chem. Lett.* 2014, 5, 2050−2057

Table 1. Modeling Results

(a) Si NWs (Surface Recombination Model)				
sample	s (cm/s)	μ (cm^2 V^{-1} s^{-1})	τ_1 (ps)	f (%)
A 30 nm (annealed)	1665 (24)	60 (0.5)		
B 90 nm (annealed)	1768 (30)	38 (0.4)		
C 90 nm	1098 (36)	13 (0.2)	144 (8)	3 (0.2)

(b) Si NCs (Triexponential Decay)					
sample	A (%)	B (%)	$C = 1 - A - B$ (%)	τ_{hc} (ps)	τ_{xx} (ps)	τ_x (ns)
6.3 nm	47 (2)	16 (2)	37	1.5 (0.1)	51 (16)	7 (2.7)

Standard deviations for the fitting parameters are shown in parentheses.

contributions from carriers residing in the bulk Si substrate and in the Si NWs.[30] While that study revealed an approach that allowed for the quantification of the dynamics and charge transport, it was not a direct measurement since prior knowledge of the substrate's electrical properties were needed. Here we disperse the NWs in a solvent prior to TRTS measurements, which allows for a direct measurement of the electrical properties of the NWs. Another technique used to extract electrical properties of NWs from TRTS is to remove them from their substrate and then transfer them to a quartz substrate.[6,31,32] However, there is the potential for wires to overlap and possibly interact, which could affect the carrier dynamics. Instead, dispersing the wires into a solvent and stirring the solution would minimize NW aggregation and ensure the measurements reflect the average response of an isolated NW.

To model the Si NC data, we employed the triexponential decay function,

$$\langle \sigma_{NC}(\tau_p) \rangle = A e^{-\tau_p/\tau_{hc}} + B e^{-\tau_p/\tau_{xx}} + C e^{-\tau_p/\tau_x} \tag{6}$$

where the three lifetimes correspond to a hot-carrier cooling and carrier–carrier recombination lifetime (τ_{hc}), an Auger (exciton–exciton annihilation) recombination lifetime (τ_{xx}), and a single exciton recombination lifetime (τ_x). The coefficients A, B, and C represent the fraction of signal associated with the lifetimes: τ_{hc}, τ_{xx}, and τ_x, respectively. For this model we impose the condition $C = 1 - A - B$. Table 1b tabulates the results. The carrier–carrier effects were examined through fluence dependent measurements (see Supporting Information), which revealed that the fast decay component decreases linearly with fluence, consistent with Auger recombination. The bulk c-Si dynamics were fit with a single exponential decay curve with a lifetime of 7 ± 3 ns.

In contrast to NWs and bulk Si, Auger recombination in nanocrystals is enhanced relative to bulk.[33] The ~50 ps Auger decay time that we observed for the NCs is consistent with literature values.[34]

Carrier Mobilities. To further understand the electrical differences of the Si nanostructures, we measured and compared $\tilde{\sigma}(\omega)$ of bulk c-Si, 30 nm Si NWs and 6.3 nm Si NCs for a variety of pump fluences (see Figure 4). When comparing $\tilde{\sigma}(\omega)$ for the nanostructures to their bulk counterpart, there is a noticeable difference in the spectra. In nanostructures, the imaginary component of the photoconductivity, $Im[\tilde{\sigma}(\omega)]$, is negative (shown as the shaded region), while the real part, $Re[\tilde{\sigma}(\omega)]$, decreases with decreasing frequency. For bulk c-Si, the data corresponds to the Drude model of conductivity. The Drude model, operative in most bulk semiconductors, is the simplest model of conductivity and treats conduction electrons as free to move

under the influence of an applied field. The model predicts a maximum value in $Re[\tilde{\sigma}(\omega)]$ at zero frequency (or dc) while $Im[\tilde{\sigma}(\omega)]$ is zero, at zero frequency, and increases with increasing frequency to a maximum, which occurs at the carrier scattering rate. In contrast to the NW and bulk c-Si data, the photoconductivity spectra for the Si NCs changes as a function of τ_p. At early delay times (500 fs), $Re[\tilde{\sigma}(\omega)]$ is nonzero and resembles that of the NW spectra, but decreases significantly by 2 ps and is completely quenched by $\tau_p = 10$ ps (Figure 4a). The $Im[\tilde{\sigma}(\omega)]$ contains only negative values and linearly decreases with increasing frequency and does not change with time (see Figure S4 in the Supporting Information). To model $\tilde{\sigma}(\omega)$, we employ the Drude–Smith theory:[35]

$$\tilde{\sigma}(\omega) = \frac{\varepsilon_0 \omega_p^2 \langle \tau \rangle}{1 - i\omega\langle\tau\rangle} \left[1 + \frac{c}{(1 - i\omega\langle\tau\rangle)} \right] \tag{7}$$

where τ is the scattering time, ω is the radial frequency, ω_p is the plasma frequency, and c is the persistence of velocity term that can range between 0 and -1. A value of -1 indicates carrier localization, and a value of 0 returns the Drude model. The plasma frequency is related to the photoinduced carrier density through $\omega_p = (Ne^2/\varepsilon_0 m^*)^{1/2}$, where N represents the carrier density, m^* is the effective mass, and e is the charge of an electron. When modeling $\tilde{\sigma}(\omega)$, we simultaneously fit the real and imaginary components using (7) and extract the mobility ($\mu = e\tau/m^*$) and carrier density for the Si NWs and bulk c-Si (Figure 4d). Representative plots of the photoconductivity for each sample are shown in Figure 4a–c.

For both the bulk c-Si and the Si NWs, we observe that the mobility decreases with increasing carrier density, implying increased carrier–carrier interactions and is consistent with the Caughey–Thomas relation.[36] The extracted mobilities for the Si NWs are similar to the measured bulk c-Si values over equivalent carrier densities. In past studies, mobility values of carriers within the Si nanostructures were found to decrease as the size of the c-Si domain decreases.[37] One cause of a reduced mobility can be linked to the carrier mean free path (l_f), which is the average distance a charge carrier travels prior to undergoing a scattering event. For bulk c-Si, l_f is on the order of 40 nm. When a nanostructure's dimensions are reduced to be on the order of or less than l_f, then the mean free path is reduced, thus decreasing the scattering time and increasing the scattering frequency. A shorter scattering time results in a lower mobility[34] ($\mu = e\langle\tau\rangle/m^*$). Therefore, if the nanostructure's characteristic size is greater than l_f, we can expect mobility values similar to that of the bulk semiconductor and for sizes below l_f the mobility will be reduced.

Figure 5 illustrates the dependence of the c parameter, which is a measure of carrier localization in the nanostructures, on the photoinduced carrier density extracted from the photo-
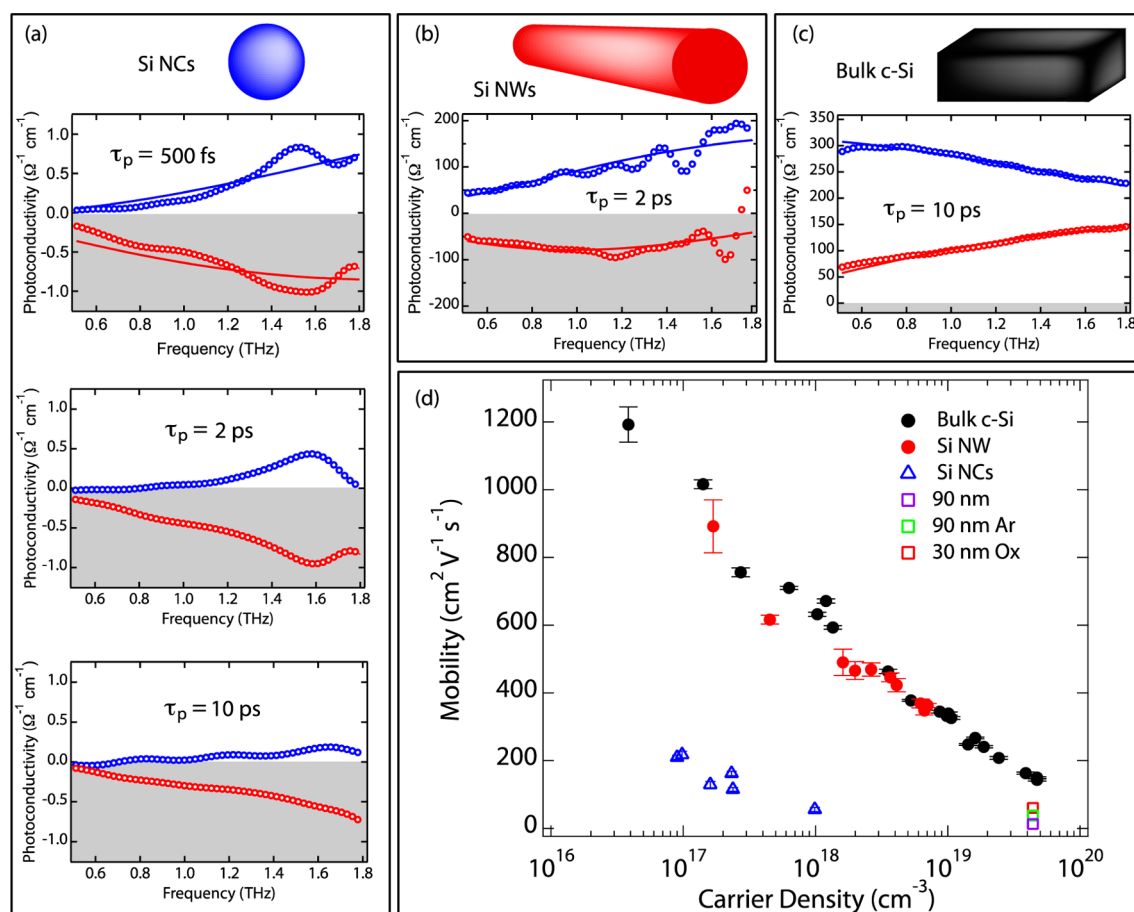
Figure 4. Panels a, b, and c, show the real (blue circles) and imaginary (red circles) parts of the photoconductivity for 6.3 nm Si NCs, 30 nm diameter Si NWs, and bulk c-Si, respectively. In panel a, we show the dependence of the complex photoconductivity as the pump–probe delay is varied. Panel d shows the extracted mobilities as a function of photoinduced carrier density for the Si NCs, Si NWs and bulk c-Si (see text). The mobilities extracted from the peak amplitudes of the Si NW time-dependent measurements are shown as open squares where the 90 nm, annealed 90, and 30 nm Si NWs are colored purple, green, and red, respectively. The solid lines shown in panels a and b represent best fits from the Drude–Smith photoconductivity model described in the text, while the solid lines in panel c represent the best fit from the unmodified Drude model.

conductivity data shown in Figure 4a,b. The linear decrease in c with carrier density observed for the Si NWs illustrates how the carriers excited in the NWs become more localized as the carrier density within the wire increases. As the carrier density increases, carrier–carrier interactions increase and thus the carrier transport will be reduced due to scattering carrier–carrier interactions and backscattering from the surface of the wire. This is in agreement with the observed trend in mobility shown in Figure 4d. For the Si NCs, on the other hand, we did not observe a dependence on carrier density. Instead, all of the extracted values for c lie between −0.99 and −1, where −1 represents complete localization.

When one dimension of the NCs is reduced to near the Bohr exciton radius (a_B), the conductivity necessarily is further modified. The Bohr radius is a parameter that describes the spatial extent of the exciton wave function in a bulk semiconductor. When the NC dimension is less than a_B, one or both of the carriers are confined, and their wave function is delocalized over the nanostructure. The free carrier motion is thus restricted by the confinement in this size regime (unless the carrier can move to a nearby NC), and in this regime the terahertz response is mainly associated with the dielectric polarization of excitons.[38] The exciton polarizability in a quantum confined structure has been measured using TRTS,[39−42] where the change in polarizability is related to a

change in the real part of the dielectric function. This can be equivalently expressed as a purely imaginary response in the conductivity over the bandwidth of our experiment. The Bohr radius for Si, defined for carriers in their lowest excited energy state, is $a_B = 4.7$ nm. For the Si NCs studied here, with a diameter of 6.3 nm, we would expect the carriers to be mostly confined, and thus expect to see a purely imaginary spectra at later delays where the exciton is no longer in an excited state. We observe this type of spectra for $\tau_p > 2$ ps, consistent with the formation of excitons in the NCs. In contrast, carriers initially excited by the 400 nm pump pulse exhibit characteristics of free-carriers ($Re[\tilde{\sigma}(\omega)] > 0$ for $\tau_p < 2$ ps), and we have extracted a mobility at $\tau_p = 500$ fs (Figure 4a). Hot-carriers (carriers with excess kinetic energy) can have much smaller wave functions depending upon the nature of the electronic structure.[43] Such carriers could result in an absorption of the terahertz probe since in this regime the electron and hole would behave more like free-carriers. Another consideration is that we are observing an off-resonant contribution to the $Re[\tilde{\sigma}(\omega)]$ response due to a broadened resonance just outside of our measurements bandwidth. This is an unlikely scenario as recent reports on ultrabroadband measurements of the complex photoconductivity of isolated Si NCs embedded in SiO_2 do not show such a resonance.[44] We therefore ascribe the initial response of the Si NCs to hot-carriers that relax to form
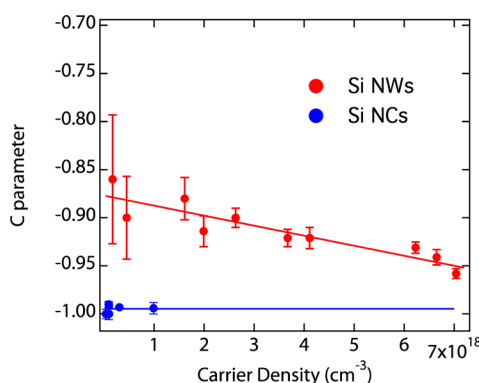
Figure 5. Dependence on carrier density of the persistence of velocity term c for the fits of the photoconductivity of the Si NW and Si NC samples from Figure 4. Solid lines are linear fits to the data.

excitons within 2 ps (fast decay in Figure 2b), thus shifting the frequency response to higher frequencies than that of the terahertz bandwidth. The exciton lifetime is similar to the carrier lifetime in bulk Si and not effected by the NC surfaces as for the NWs. The long lifetime is consistent with the high PL QYs observed for Si NC and is an indication of the well-passivated, high quality NCs prepared by plasma synthesis.[45]

In conclusion, we have measured the photoconductivity of isolated Si nanowires and nanocrystals. In contrast to the carrier dynamics of bulk Si and Si NCs, we find that the carrier dynamics of Si NWs are dominated by the NW surface. Annealing increases the carrier mobility within the NW at the expense of higher surface recombination velocities, which we ascribe to movement of Au from the core of the wires to their surfaces. We have also measured the time-resolved electrical properties of isolated Si NCs. The ultrafast carrier-dynamics of the Si NCs reveal that hot-carriers are initially created in the NC, which then cool over a period of ∼2 ps, after which excitons are formed. The carrier dynamics show a multiple exciton lifetime of ∼50 ps followed by a long-lived exciton (>7 ns). Mobility values of the hot-carriers initially created in the NC were extracted from frequency-dependent photoconductivity measurements for a variety of carrier densities.

■ ASSOCIATED CONTENT

Ⓢ Supporting Information
Additional experimental details. This material is available free of charge via the Internet at http://pubs.acs.org.

■ AUTHOR INFORMATION

Notes
The authors declare no competing financial interest.

■ ACKNOWLEDGMENTS

■ REFERENCES

(1) Wheeler, D. A.; Huang, J.-A.; Newhouse, R. J.; Zhang, W.-F.; Lee, S.-T.; Zhang, J. Z. Ultrafast Exciton Dynamics in Silicon Nanowires. *J. Phys. Chem. Lett.* **2012**, *3*, 766−771.

(2) Fuzell, J.; Thibert, A.; Atkins, T. M.; Dasog, M.; Busby, E.; Veinot, J. G. C.; Kauzlarich, S. M.; Larsen, D. S. Red States versus Blue States in Colloidal Silicon Nanocrystals: Exciton Sequestration into Low-Density Traps. *J. Phys. Chem. Lett.* **2013**, *4*, 3806−3812.

(3) Hessel, C. M.; Reid, D.; Panthani, M. G.; Rasch, M. R.; Goodfellow, B. W.; Wei, J.; Fujii, H.; Akhavan, V.; Korgel, B. A. Synthesis of Ligand-Stabilized Silicon Nanocrystals with Size-Dependent Photoluminescence Spanning Visible to Near-Infrared Wavelengths. *Chem. Mater.* **2011**, *24*, 393−401.

(4) Mangolini, L.; Thimsen, E.; Kortshagen, U. High-Yield Plasma Synthesis of Luminescent Silicon Nanocrystals. *Nano Lett.* **2005**, *5*, 655−659.

(5) Wheeler, L. M.; Neale, N. R.; Chen, T.; Kortshagen, U. R. Hypervalent Surface Interactions for Colloidal Stability and Doping of Silicon Nanocrystals. *Nat. Commun.* **2013**, *4*, 2197.

(6) Tang, H.; Zhu, L.-G.; Zhao, L.; Zhang, X.; Shan, J.; Lee, S.-T. Carrier Dynamics in Si Nanowires Fabricated by Metal-Assisted Chemical Etching. *ACS Nano* **2012**, *6*, 7814−7819.

(7) Bergren, M. R.; Simonds, B. J.; Yan, B.; Yue, G.; Ahrenkiel, R.; Furtak, T. E.; Collins, R. T.; Taylor, P. T.; Beard, M. C. Electron Transfer in Hydrogenated Nanocrystalline Silicon Observed by Time-Resolved Terahertz Spectroscopy. *Phys. Rev. B* **2013**, *87*, 081301(R).

(8) Cooke, D.; Macdonald, A.; Hryciw, A.; Meldrum, A.; Wang, J.; Li, Q.; Hegmann, F. Ultrafast Terahertz Conductivity of Photoexcited Nanocrystalline Silicon. *J. Mater. Sci.: Mater. Electron.* **2007**, *18*, 447−452.

(9) Allen, J. E.; Hemesath, E. R.; Perea, D. E.; Lensch-Falk, J. L.; Li, Z. Y.; Yin, F.; Gass, M. H.; Wang, P.; Bleloch, A. L.; Palmer, R. E.; et al. High-Resolution Detection of Au Catalyst Atoms in Si Nanowires. *Nat. Nanotechnol.* **2008**, *3*, 168−173.

(10) Dan, Y.; Seo, K.; Takei, K.; Meza, J. H.; Javey, A.; Crozier, K. B. Dramatic Reduction of Surface Recombination by in Situ Surface Passivation of Silicon Nanowires. *Nano Lett.* **2011**, *11*, 2527−2532.

(11) Kelzenberg, M. D.; Turner-Evans, D. B.; Kayes, B. M.; Filler, M. A.; Putnam, M. C.; Lewis, N. S.; Atwater, H. A. Photovoltaic Measurements in Single-Nanowire Silicon Solar Cells. *Nano Lett.* **2008**, *8*, 710−714.

(12) Klimov, V. I.; Schwarz, C. J.; McBranch, D. W.; White, C. W. Initial Carrier Relaxation Dynamics in Ion-Implanted Si Nanocrystals: Femtosecond Transient Absorption Study. *Appl. Phys. Lett.* **1998**, *73*, 2603−2605.

(13) Demichel, O.; Calvo, V.; Besson, A.; Noé, P.; Salem, B.; Pauc, N.; Oehler, F.; Gentile, P.; Magnea, N. Surface Recombination Velocity Measurements of Efficiently Passivated Gold-Catalyzed Silicon Nanowires by a New Optical Method. *Nano Lett.* **2010**, *10*, 2323−2329.

(14) Demichel, O.; Calvo, V.; Pauc, N.; Besson, A.; Noé, P.; Oehler, F.; Gentile, P.; Magnea, N. Recombination Dynamics of Spatially Confined Electron−Hole System in Luminescent Gold Catalyzed Silicon Nanowires. *Nano Lett.* **2009**, *9*, 2575−2578.

(15) Cui, H.; Wang, C. X.; Yang, G. W. Origin of Self-Limiting Oxidation of Si Nanowires. *Nano Lett.* **2008**, *8*, 2731−2737.

(16) Anthony, R.; Kortshagen, U. Photoluminescence Quantum Yields of Amorphous and Crystalline Silicon Nanoparticles. *Phys. Rev. B* **2009**, *80*, 115407.

(17) Iwaszczuk, K.; Cooke, D. G.; Fujiwara, M.; Hashimoto, H.; Uhd Jepsen, P. Simultaneous Reference and Differential Waveform

2056

dx.doi.org/10.1021/jz500863a | *J. Phys. Chem. Lett.* 2014, 5, 2050−2057

Acquisition in Time-Resolved Terahertz Spectroscopy. *Opt. Express* **2009**, *17*, 21969−21976.

(18) Beard, M. C.; Blackburn, J. L.; Heben, M. J. Photogenerated Free Carrier Dynamics in Metal and Semiconductor Single-Walled Carbon Nanotube Films. *Nano Lett.* **2008**, *8*, 4238−4242.

(19) Kužel, P.; Kadlec, F.; Němec, H. Propagation of Terahertz Pulses in Photoexcited Media: Analytical Theory for Layered Systems. *J. Chem. Phys.* **2007**, *127*, 024506.

(20) Beard, M. C.; Schmuttenmaer, C. A. Using the Finite-Difference Time-Domain Pulse Propagation Method to Simulate Time-Resolved THz Experiments. *J. Chem. Phys.* **2001**, *114*, 2903−2909.

(21) Grischkowsky, D.; Keiding, S. r.; Exter, M. v.; Fattinger, C. Far-Infrared Time-Domain Spectroscopy with Terahertz Beams of Dielectrics and Semiconductors. *J. Opt. Soc. Am. B* **1990**, *7*, 2006−2015.

(22) Pedersen, J. E.; Keiding, S. R. THz Time-Domain Spectroscopy of Nonpolar Liquids. *IEEE J. Quantum Elect.* **1992**, *28*, 2518−2522.

(23) Giordano, S. Effective Medium Theory for Dispersions of Dielectric Ellipsoids. *J. Electrostat.* **2003**, *58*, 59−76.

(24) Öğüt, S.; Chelikowsky, J. R.; Louie, S. G. Quantum Confinement and Optical Gaps in Si Nanocrystals. *Phys. Rev. Lett.* **1997**, *79*, 1770−1773.

(25) McKelvey, J. P. Volume and Surface Recombination of Injected Carriers in Cylindrical Semiconductor Ingots. *IRE Trans. Electron Devices* **1958**, *5*, 260−264.

(26) Bailly, A.; Renault, O.; Barrett, N.; Zagonel, L. F.; Gentile, P.; Pauc, N.; Dhalluin, F.; Baron, T.; Chabli, A.; Cezar, J. C.; et al. Direct Quantification of Gold along a Single Si Nanowire. *Nano Lett.* **2008**, *8*, 3709−3714.

(27) den Hertog, M. I.; Rouviere, J.-L.; Dhalluin, F.; Desré, P. J.; Gentile, P.; Ferret, P.; Oehler, F.; Baron, T. Control of Gold Surface Diffusion on Si Nanowires. *Nano Lett.* **2008**, *8*, 1544−1550.

(28) Kerr, M. J.; Cuevas, A. General Parameterization of Auger Recombination in Crystalline Silicon. *J. Appl. Phys.* **2002**, *91*, 2473−2480.

(29) Hangleiter, A. Nonradiative Recombination via Deep Impurity Levels in Silicon: Experiment. *Phys. Rev. B* **1987**, *35*, 9149−9161.

(30) Ulbricht, R.; Kurstjens, R.; Bonn, M. Assessing Charge Carrier Trapping in Silicon Nanowires Using Picosecond Conductivity Measurements. *Nano Lett.* **2012**, *12*, 3821−3827.

(31) Joyce, H. J.; Docherty, C. J.; Gao, Q.; Tan, H. H.; Jagadish, C.; Lloyd-Hughes, J.; Herz, L. M.; Johnston, M. B. Electronic Properties of GaAs, InAs and InP Nanowires Studied by Terahertz Spectroscopy. *Nanotechnology* **2013**, *24*, 214006.

(32) Strait, J. H.; George, P. A.; Levendorf, M.; Blood-Forsythe, M.; Rana, F.; Park, J. Measurements of the Carrier Dynamics and Terahertz Response of Oriented Germanium Nanowires using Optical-Pump Terahertz-Probe Spectroscopy. *Nano Lett.* **2009**, *9*, 2967−2972.

(33) Klimov, V. I.; Mikhailovsky, A. A.; Xu, S.; Malko, A.; Hollingsworth, J. A.; Leatherdale, C. A.; Eisler, H. J.; Bawendi, M. G. Optical Gain and Stimulated Emission in Nanocrystal Quantum Dots. *Science* **2000**, *290*, 314−317.

(34) Beard, M. C.; Knutsen, K. P.; Yu, P.; Luther, J. M.; Song, Q.; Metzger, W. K.; Ellingson, R. J.; Nozik, A. J. Multiple Exciton Generation in Colloidal Silicon Quantum Nanocrystals. *Nano Lett.* **2007**, *7*, 2506−2512.

(35) Smith, N. V. Classical Generalization of the Drude Formula for the Optical Conductivity. *Phys. Rev. B* **2001**, *64*, 155106.

(36) Caughey, D. M.; Thomas, R. E. Carrier Mobilities in Silicon Empirically Related to Doping and Field. *Proc. IEEE* **1967**, *55*, 2192−2193.

(37) Wang, Y. C.; Ahn, H.; Chuang, C. H.; Ku, Y. P.; Pan, C. L. Grain-Size-Related Transient Terahertz Mobility of Femtosecond-Laser-Annealed Polycrystalline Silicon. *Appl. Phys. B: Laser Opt.* **2009**, *97*, 181−185.

(38) Hendry, E.; Schins, J. M.; Candeias, L. P.; Siebbeles, L. D. A.; Bonn, M. Efficiency of Exciton and Charge Carrier Photogeneration in a Semiconducting Polymer. *Phys. Rev. Lett.* **2004**, *92*, 196601.

(39) Ulbricht, R.; Pijpers, J. J. H.; Groeneveld, E.; Koole, R.; Donega, C. d. M.; Vanmaekelbergh, D.; Delerue, C.; Allan, G.; Bonn, M. Loosening Quantum Confinement: Observation of Real Conductivity Caused by Hole Polarons in Semiconductor Nanocrystals Smaller than the Bohr Radius. *Nano Lett.* **2012**, *12*, 4937−4942.

(40) Wang, F.; Shan, J.; Islam, M. A.; Herman, I. P.; Bonn, M.; Heinz, T. F. Exciton Polarizability in Semiconductor Nanocrystals. *Nat. Mater.* **2006**, *5*, 861−864.

(41) Dakovski, G. L.; Lan, S.; Xia, C.; Shan, J. Terahertz Electric Polarizability of Excitons in PbSe and CdSe Quantum Dots. *J. Phys. Chem. C* **2007**, *111*, 5904−5908.

(42) Pijpers, J. J. H.; Milder, M. T. W.; Delerue, C.; Bonn, M. (Multi)exciton Dynamics and Exciton Polarizability in Colloidal InAs Quantum Dots. *J. Phys. Chem. C* **2010**, *114*, 6318−6324.

(43) Cho, B.; Peters, W. K.; Hill, R. J.; Courtney, T. L.; Jonas, D. M. Bulklike Hot Carrier Dynamics in Lead Sulfide Quantum Dots. *Nano Lett.* **2010**, *10*, 2498−2505.

(44) Cooke, D. G.; Meldrum, A.; Uhd Jepsen, P. Ultrabroadband Terahertz Conductivity of Si Nanocrystal Films. *Appl. Phys. Lett.* **2012**, *101*, 211107.

(45) Kortshagen, U. Nonthermal Plasma Synthesis of Semiconductor Nanocrystals. *J. Phys. D: Appl. Phys.* **2009**, *42*, 113001.